Nigrostriatal iron accumulation in the progression of Parkinson's disease

Check for updates

M. López-Aguirre[1,2,3,4], T. Balzano [1,2], M.H.G. Monje [1,2], N. Esteban-García[1,2,5],
R. Martínez-Fernández [1,2], N.L. Del Rey [1,2,5], M. Ciorraga[1,2], A. Sánchez-Ferro [1,2,6,7],
I. Trigo-Damas [1,2,4,8], J. Blesa[1,2,4,8], J. A. Obeso [1,2,4,9] & J. A. Pineda-Pardo [1,2] ✉

Iron deposition in the nigrostriatal system plays a pivotal role in Parkinson's disease (PD) onset and progression. This study explored the time course of nigrostriatal iron accumulation in 54 PD patients at early to moderately advanced stages and 20 age-matched healthy controls. Using multi-echo T2*-MRI and R2* relaxometry, iron content was assessed in the substantia nigra pars compacta (SNpc) and striatum. In vivo findings were contrasted with histological analyses in a progressive 1-methyl-4-phenyl-1,2,3,6-tetrahydropyridine-induced parkinsonism model involving six non-human primates (NHPs) and two controls using Perls' Prussian blue staining. Complementarily, dopaminergic degeneration was quantified by 6-[^{18}F]-fluoro-L-dopa PET in humans and TH immunohistochemistry in NHPs. Results showed progressive iron accumulation in the SNpc correlating with striatal dopaminergic denervation and neuronal loss. Striatal iron followed a V-shaped progression, decreasing initially and increasing later. Iron in the SNpc may serve as a marker of neurodegeneration in PD, while decreased striatal iron may indicate pathological susceptibility to dopaminergic loss.

The primary hallmark of Parkinson's disease (PD) is the progressive loss of dopaminergic neurons within the substantia nigra (SN) pars compacta (SNpc)[1–4], a neurodegenerative process frequently related to disruptions in iron metabolism[5,6]. In this regard, iron is essential for the correct function of numerous physiological processes, including dopamine synthesis and metabolism[6]. However, iron accumulation in its free radical form has a potential neurotoxic role due to its redox-active behavior[6], which promotes formation of reactive oxygen species that may damage cellular DNA via oxidative stress, ultimately leading to neuronal death[7–9].

In PD, increased iron has been confirmed within the SN through a myriad of techniques including histochemistry[10], transcranial sonography[11], and MRI[12–14], suggesting it is a potential biomarker for neurodegeneration[5,13–15]. It is still uncertain, though, if iron accumulation in the SNpc is triggered before or after the onset of PD and how it develops during PD progression[6,16]. Moreover, it is still a matter of debate if increased iron deposition is a cause or a consequence of neurodegeneration in PD, or even an effect associated with anti-parkinsonian drugs[16–18]. On the other hand, less emphasis has been placed on striatal iron, and reports show heterogeneous results[12,16,19,20]. Nevertheless, studies conducted in rodents have found correlations between brain iron deficiency and alterations in dopaminergic function[21–23], suggesting that iron deficits might play an important role during the initial striatal dopaminergic dysfunction[24]. Indeed, some recent MRI studies have described reduced striatal iron content in de novo PD populations[16,25]. Thus, elucidating the features of striatal and SNpc iron deposition during the early stages of PD holds promise for a better understanding of PD development and disease progression.

Here we studied iron progression patterns within the nigrostriatal system, spanning from early to moderate stages of PD. To achieve this, we employed R2* relaxometry MRI, a commonly used technique to identify iron alterations within the nigrostriatal system[12,13,19,25,26] due to its ability to directly capture iron load changes[27]. Furthermore, to validate our in vivo MRI findings, and to explore the relations between iron alterations and dopaminergic degeneration, iron was assessed histologically in non-human primates (NHP) at different stages of neurodegeneration using the 1-methyl-4-phenyl-1,2,3,6-tetrahydropyridine (MPTP) parkinsonian model[28,29].

[1]HM CINAC (Centro Integral de Neurociencias Abarca Campal), Hospital Universitario HM Puerta del Sur, HM Hospitales, Madrid, Spain. [2]Instituto de Investigación Sanitaria HM Hospitales, Madrid, Spain. [3]PhD Program in Physics, Complutense University of Madrid, Madrid, Spain. [4]Centro de Investigación Biomédica en Red de Enfermedades Neurodegenerativas (CIBERNED), Instituto de Salud Carlos III, Madrid, Spain. [5]PhD Program in Neuroscience, Universidad Autónoma de Madrid-Cajal Institute, Madrid, Spain. [6]Department of Neurology, Hospital Universitario 12 de Octubre, Madrid, Spain. [7]Department of Medicine, Complutense University of Madrid, Madrid, Spain. [8]Facultad HM de Ciencias de la Salud de la Universidad Camilo José Cela, Madrid, Spain. [9]Universidad San Pablo-CEU, Madrid, Spain. ✉e-mail: jpineda.hmcinac@hmhospitales.com

Results

R2* relaxometry MRI was acquired to assess iron content alterations in a cohort of PD patients compared with healthy controls (HC). PD patients were categorized into de novo (dn-PD), early (mild-PD), or moderate (mod-PD) groups according to their clinical evaluation (MDS-UPDRS part III) and time of disease progression (see methods). Iron-sensitive R2* maps were assessed in multiple regions of interest (ROIs) within the nigrostriatal system to evaluate the topography of iron alterations on the more-affected (MAS) and less-affected (LAS) sides. Analogously, histological analyses of iron content were performed in the same set of regions in a single hemisphere. For histology, the SNpc was segmented as a single ROI, whereas in MRI this was divided in anteromedial and posterolateral ROIs. NHPs were segregated according to nigrostriatal degeneration into control or MPTP groups in stages 1-to-3.

Iron content alterations in the nigrostriatal system

Nigral iron progressively increased along with disease stage in PD patients in both hemispheres, MAS and LAS (Fig. 1a). This increment did not reach significance at dn-PD stage as compared to HC, although a trend was observed in the anteromedial SNpc in the MAS ($P < 0.1$; $K > 0$; $d = 0.59$). In mild-PD, iron accumulation reached weak significant evidence in the anteromedial SNpc region ($P < 0.05$; $K > 0$; $d = 0.80$ vs HC), also extending to the opposite hemisphere at mod-PD stage ($P < 0.05$; $K > 0$; $d = 0.70$). In the posterolateral SNpc a bilateral and strongly significant evidence was found, but only in the most advanced stage of the disease ($P < 0.01$; $K > 1$; $d > 1.10$ against HC). Quantification of histological data from processed Perls' Prussian blue (PPB) stained sections was conducted using relative integrated density (RID), a new metric that combines area percent (AP) and optical density (OD) measurements into a single value that is normalized to controls (see methods). In the SNpc (Fig. 1b), RID revealed a gradual increase in iron as animals displayed greater neuronal death (mean RID = 1.00/1.07/1.39/1.60). This observation is mainly driven by the AP metric, as OD remains stable across stages (Supplementary Fig. 1).

In the striatum, comparisons between dn-PD and HC groups exhibited decreased magnitude of iron concentration in all caudate and putamen subregions, while they only reached moderate significance in the caudate in the MAS ($P < 0.05$; $K > 0.5$; $d > 0.72$) (Fig. 2a). These differences in the caudate vanished in mild-PD and mod-PD groups. The initial reduction of iron in dn-PD subjects was reversed on later stages on the MAS, showing a progressive increase thereafter that reached moderate-to-strong significance between mod-PD and dn-PD patients in the caudate ($P < 0.05$; $K > 0.5$; $d = 0.97/0.85$ in anterior/posterior ROIs) and the posterior putamen ($P < 0.05$; $K > 0.5$; $d = 0.76$) (Fig. 2a). In the histological analysis, stage-1 animals exhibited a global iron loss compared to controls (RID = 0.62/0.53 in anterior/posterior caudate and RID = 0.71/0.56 in anterior/posterior putamen) (Fig. 2b). Following this initial loss, stage-2 and stage-3 animals showed higher values than the stage-1 group, reaching similar values in the striatum to control animals (RID = [1.01,1.25] and RID = [0.66,0.95] for stage-2 and stage-3 animals, respectively). Both effects, i.e., the initial decay

and the posterior recovery are also observed in both AP and OD metrics (Supplementary Fig. 1).

Correlation between iron content and dopaminergic degeneration

The relationship between iron accumulation in the SNpc and nigrostriatal dopaminergic integrity was explored by correlation analyses in both in vivo human and ex vivo primate cohorts (see Fig. 3). Dopaminergic status in PD subjects was quantified by PET imaging using the 6-[^{18}F]-fluoro-L-dopa (FDOPA) influx rate (K_i). This metric was estimated in the SNpc and the putamen for dn-PD and mild-PD cohorts. In the MAS, these analyses revealed a moderately significant negative correlation between R2* in the SNpc and FDOPA K_i in the putamen ($\rho_{Sp} = -0.32$; $P < 0.05$; $K > 0.5$), while in the SNpc this relationship was marginal ($\rho_{Sp} = -0.27$; $P < 0.10$; $K > 0$). No significant correlations were found in the LAS or when comparing striatal R2* with nigrostriatal FDOPA K_i assessments. In primates, striatal TH quantification was used as a marker of dopaminergic integrity. Analyses in ex vivo data (Fig. 3b) revealed a moderately significant negative correlation between nigral RID and striatal TH quantification by OD ($\rho_{Sp} = -0.83$; $P = 0.015$; $K > 0.5$). Homologous findings, but with lower evidence, were seen when comparing RID values with the number of surviving cells within the SNpc ($\rho_{Sp} = -0.81$, $P = 0.022$; $K > 0$). These were also observed with AP and OD metrics (Supplementary Fig. 2). No correlations were found between striatal RID and striatal dopaminergic dysfunction or neuronal count.

Spatial distribution of iron accumulation in the nigrostriatal system

To dig into the spatial distribution of iron accumulation, SNpc and striatal structures were partitioned into slices of equal thickness along their main axis determined by spatial principal component analysis (PCA)[30,31]. The SNpc exhibited a progressive and spatially homogeneous increment of iron in both hemispheres (Fig. 4). In the MAS, dn-PD exhibited lower R2* values at both ends in the caudate (anterior and posterior). In contrast, at the mod-PD stage, this pattern was reversed relative to dn-PD and mild-PD, with values returning to levels comparable to those observed in HC. In the putamen, the mod-PD group showed increased R2* compared to dn-PD and mild-PD but only at the posterior end. In the LAS, alterations in striatal R2* were less pronounced than in the MAS. However, two clusters of increased iron concentration were identified between mod-PD and dn-PD, located in the posterior caudate and the anterior putamen of this hemisphere.

Discussion

In this study, we characterized the progression of iron content in vivo in a cohort of PD patients from de novo to moderate severity stages using R2* relaxometry MRI. These results were further examined neuropathologically in NHPs treated with the neurotoxin MPTP to induce nigrostriatal dopaminergic degeneration. Overall, we demonstrated the existence of distinct time courses of iron alteration in the SNpc and the striatum. In the SNpc,

Fig. 1 | Evolution of iron content in the substantia nigra pars compacta (SNpc). a Boxplots illustrating R2* relaxometry values for healthy controls (green) and de novo, mild and moderate PD subjects (yellow, orange, and red, respectively). Symbols denote inter-group differences, and the strength of those differences is indicated as: $P > 0.05$ or $K < 0$ (no symbol), $P < 0.05$ and $K \geq 0$ (~), $P < 0.05$ and $0.5 < K \leq 1$ (*); $P \leq 0.01$ and $K > 1$ (**). MAS More affected Side, LAS Less affected side. **b** Bar graph displaying the histochemical quantification of iron in the macaque MPTP model. Crosses denote the relative integrated density quantified from Perls' Prussian blue (PPB) staining for each animal.
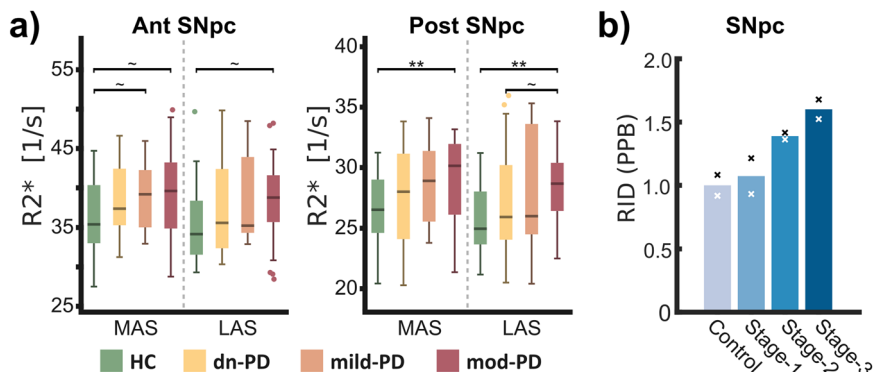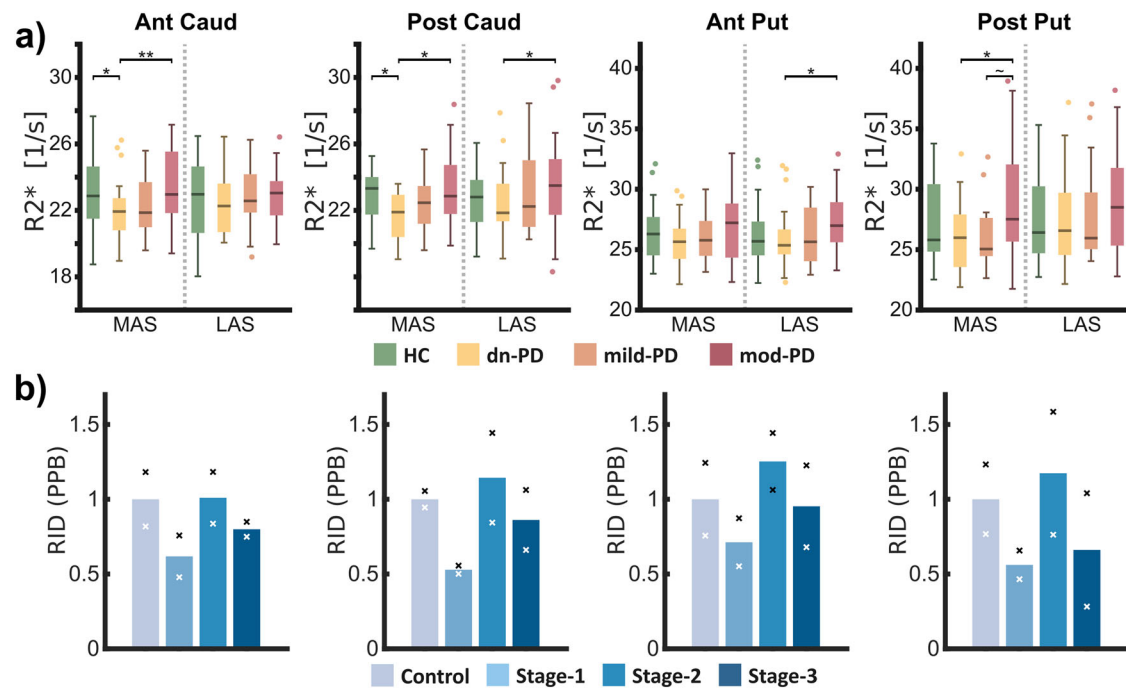
Fig. 2 | Evolution of iron content in the caudate nucleus (Caud) and putamen (Put). a Boxplots illustrating R2* relaxometry values for healthy controls (green) and de novo, mild, and moderate PD subjects (yellow, orange, and red, respectively). Symbols denote inter-group differences, and the strength of those differences is indicated as: $P > 0.05$ or $K < 0$ (no symbol), $P < 0.05$ and $K \geq 0$ (~), $P < 0.05$ and $0.5 < K \leq 1$ (*); $P \leq 0.01$ and $K > 1$ (**). MAS More affected Side, LAS Less affected side. **b** Bar graph displaying the histochemical quantification of iron in the macaque MPTP model. Crosses denote the relative integrated density quantified from Perls' Prussian blue (PPB) staining for each animal ($n = 2$ per group).
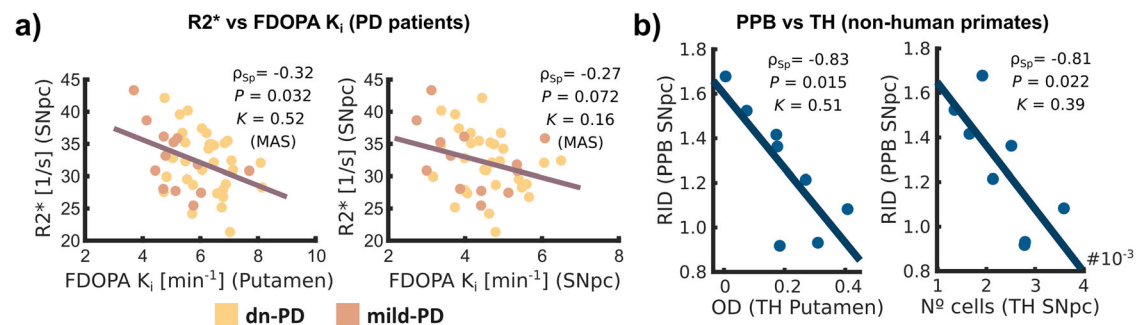

Fig. 3 | Spearman correlation analysis showing the relation between the increase of iron in the SNpc and dopaminergic degeneration in the putamen and the SNpc. a R2* relaxometry MRI vs FDOPA Ki in PD patients. Yellow and orange, respectively, denote de novo and mild PD subjects. **b** Perls' Prussian blue (PPB) vs TH in non-human primates.

iron accumulation increased with disease progression. This increase directly correlated with the loss of TH+ neurons and dopaminergic denervation of the striatum in NHPs, and with the loss of striatal FDOPA PET uptake in PD patients. In contrast, striatal iron exhibited a V-shaped time course with disease progression and MPTP stages, showing an initial decrease in de novo PD patients and asymptomatic animals, which was reversed in more advanced stages.

Nigral iron levels were significantly elevated in both PD patients and MPTP-intoxicated macaques consistent with previous reports, using MRI[12–14,32–35] or histology[10,36–40]. The main contributor to iron increment in the SNpc is probably neuronal death[41]. Our data further support this statement, showing a strong correlation between MPTP-induced neurodegeneration (TH+ neuronal loss and striatal dopaminergic denervation) and increased SNpc iron concentration. Nevertheless, in addition to neurodegeneration, other mechanisms might lead to nigral iron accumulation

in PD. These include enhanced iron influx via divalent metal transporter 1[42], a marked reduction in neuronal iron storage capacity[43–45], and a potential downregulation of neuronal ability to clear iron[45–47]. Still, the question remains as to whether iron accumulation precedes or is just a consequence of neuronal death. Yet, it is quite possible that both phenomena, i.e., iron content increasing upon neuronal death and iron overload inducing further tissular damage, occur simultaneously[6,48]. Further investigations are necessary to understand the neuronal susceptibility to iron and the triggers for its accumulation.

Contrary to what has been reported on nigral iron in PD, existing reports on striatal iron content show heterogeneous findings. While some studies have described an absence of alterations in the region[12,13,15,34,49–52], others have documented significant increments, or even reductions, compared to HC[19,25,53–58]. Interestingly, our results describe a V-shaped time course for iron concentration in the striatum, which may, at least in part,
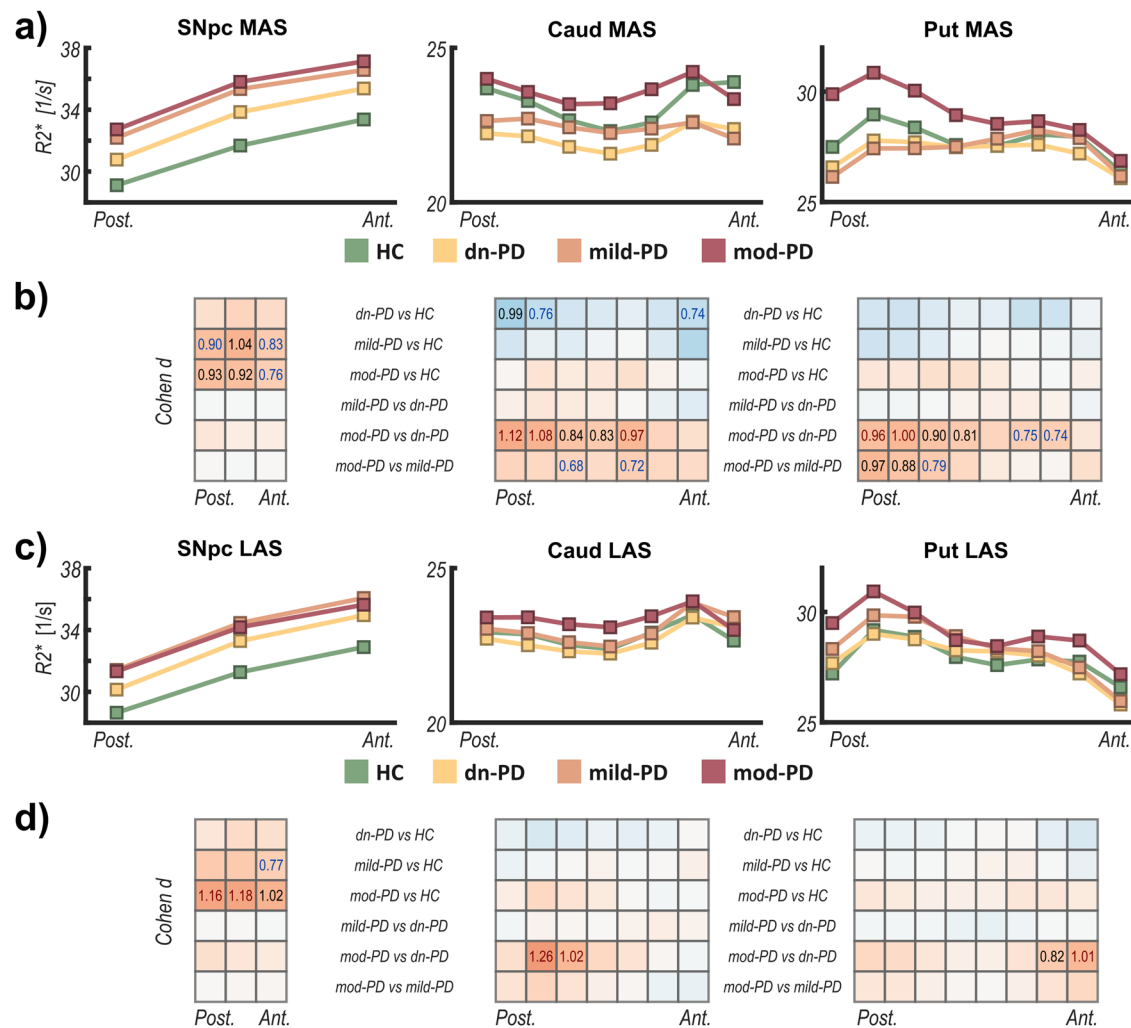
Fig. 4 | Spatial distribution of the iron content across the main PCA axis (posterior-to-anterior). From left to right are displayed the SNpc, the caudate, and the putamen. **a** and **c** display the mean R2* values across the main PCA axis in the more affected side (MAS) or the less affected side (LAS). Healthy controls are illustrated in green and de novo, mild, and moderate PD subjects are shown in yellow, orange, and red, respectively. **b** and **d** exhibit the effect size (Cohen d) of the inter-group comparisons. Cohen d values are displayed only when these comparisons reached weak ($P < 0.05$ and $K \geq 0$, blue), moderate ($P < 0.05$ and $0.5 < K \leq 1$, black) or strong ($P \leq 0.01$ and $K > 1$, red) significance. Background color indicates the trend of these changes, i.e., blue denotes a reduction in iron and red and increment.

explain these heterogeneous findings. Admittedly, an early reduction in iron concentration in the context of a progressive neurodegenerative disease might seem counterintuitive. Yet, this phenomenon remains consistent in both our patient cohort and the macaque MPTP model, aligning with findings from two prior reports in de novo PD patients[16,25]. The role and relevance of this reduction is, however, unknown. Epidemiological studies have established some causal relationships between systemic iron deficiencies and increased risk of developing PD[59–64]. Furthermore, iron deficits have been specifically related to severe dopaminergic dysfunction in animal models, either by constraining systemic iron intake[21–23,65] or by suppressing neuronal iron uptake[24]. Moreover, it is well known that iron plays a fundamental role in dopamine synthesis and metabolism[6], and thus, it is likely that early dopaminergic dysfunction modulates nigrostriatal iron dynamics. In line with this, our topographical analysis of iron concentration, along the posterior-to-anterior striatal axis, revealed specific clusters of iron alterations in the posterior region of the putamen, which coincides with the characteristic topography of dopaminergic depletion in PD[54,66–69]. This provides further evidence for the close relationship between these processes along with nigrostriatal degeneration. Probably, early dopaminergic denervation could lead to a reduced iron demand and storage capacity at striatal terminals. These findings may explain why a recent disease-modifying clinical trial centered on reducing nigrostriatal iron was

unsuccessful[70]. This randomized placebo-controlled trial reported a reduction in the iron load in both the SNpc and the striatum, but it also showed clinical worsening in the arm receiving the iron chelator. Therefore, while the selected drug may preserve neuronal soma in the SN by blocking iron-associated oxidative stress mechanisms, the unexpected clinical worsening might be related to an iron deficit at the striatal terminals that could exacerbate dopaminergic dysfunction.

The trend of decreasing striatal iron is reversed with disease progression, a result that cannot be explained by dopaminergic dysfunction. Several hypotheses might explain this phenomenon. For example, dopaminergic compensatory mechanisms are known to stimulate dopaminergic function in surviving dopaminergic neurons[71–73], so they could also be increasing iron demands at striatal terminals and lead to upregulation of iron transport into the region. Yet, these compensatory mechanisms are not fully active in asymptomatic MPTP macaques[72] and may still be partially active in the de novo PD group. Therefore this would explain the delayed reversal in the iron accumulation trend. In addition to compensatory mechanisms, levodopa intake may promote iron transport to dopaminergic terminals by stimulating dopamine synthesis in surviving dopaminergic neurons[74]. However, this does not explain the outcomes observed in the macaque group, as they did not receive levodopa. Finally, imbalances in iron homeostasis contributing to neurodegeneration may originate not only from neurons but

also from glial cells, which are the most iron-rich cells in the brain[75,76]. Nigrostriatal presynaptic axonal pruning may promote astrocytosis, triggering iron accumulation through upregulation of iron influx and efflux mechanisms[77]. Moreover, it has been shown that the glial response to nigrostriatal neurodegeneration is both region- and time-dependent[78], suggesting that delayed iron accumulation in the striatum could result from late glial activation in this region. Consequently, while the initial loss of iron in the striatum is likely to be associated with dopaminergic degeneration, its subsequent progressive accumulation may be driven by a sustained glial response[79].

Some limitations should be acknowledged for the results presented here. First, our sample size is not very large, especially for the mild-PD group. Still, we carefully selected the recruited groups, including only young subjects without major comorbidities who had predominantly motor signs and a focal presentation. We believe this choice has reduced heterogeneity and confounding factors. In our dataset, since the PD groups were age-matched, the impact of aging on iron accumulation is not thought to be a consideration. However, aging is a significant factor in brain iron accumulation[80–82]. Therefore, longer follow-ups and longitudinal studies with age-matched HC are necessary to fully characterize the effects of striatal iron on PD progression. Since our animal sample size is limited to two per group, our findings should also be interpreted with caution. Further studies with larger animal cohorts could be undertaken to conclusively verify these findings. In addition, all stages of neurodegeneration in monkeys are reached in a short period of time, in contrast to the progression of PD, which might take several years to reach the same stage. Thus, natural compensatory mechanisms may develop to a lesser extent in MPTP-treated monkeys. Finally, although R2* is known to mainly reflect iron concentration[27,83], part of the signal is non-iron dependent. Changes in water content, brain oxygenation, or surrounding diamagnetic elements, such as myelin or calcium, might affect R2* sensitivity to iron content alterations[15,84–86]. Post-processing techniques that minimize susceptibility disturbances induced by surrounding components, like QSM, may be more accurate than R2* in characterizing iron[15,87,88], although they come with their own drawbacks. In QSM, brain magnetic susceptibilities are typically calculated using a reference region to establish the zero-susceptibility value (e.g.: CSF of the ventricles or a whole brain mask)[88]. This technical aspect could pose a major limitation when studying conditions characterized by widespread changes in brain iron content, as in PD[59–61,89]. In such cases, it may be challenging to identify a consistent reference region that remains unaffected throughout disease progression. Consequently, these techniques may not be suitable for examining iron alterations in pathologies of this nature, leaving R2* as a more suitable option.

In conclusion, we have found distinct iron accumulation patterns in the SNpc and striatum by using MRI and histology to offer valuable insights into the pathophysiological mechanisms underlying early PD. As consistently reported, iron accumulation was found to be progressively increased in the SNpc and was directly linked to nigrostriatal neurodegeneration. In contrast, striatal iron displayed a V-shaped pattern that overlaps with the topography of dopaminergic depletion. Therefore, we conclude that early iron deficiency within the striatum may be linked with the onset of dopaminergic depletion in PD, potentially offering a target for the development of new preventive or disease-modifying therapies. Nevertheless, further investigation is necessary to definitively establish the link between striatal iron concentration and dopaminergic denervation in PD.

Methods
Human cohorts
Fifty-four PD patients and twenty HC were enrolled between February 2016 and October 2020 at the University Hospital HM Puerta del Sur (Móstoles, Spain). PD subjects, selected from previous studies[68,90,91], were classified into three different cohorts: (a) 28 de novo PD (dn-PD) patients with less than 12 months after diagnosis and showing unilateral and minor motor impairment. All patients were levodopa-naive at the time of recruitment; however 11 were medicated with rasagiline, 3 with dopamine agonists (rotigotine patch, pramipexole, ropirinole), and 4 with a combination of rasagiline and dopamine agonists; (b) 15 PD subjects longitudinally followed from the dn-PD group up to 3 years with mild signs (mild-PD); (c) 26 PD patients with moderate parkinsonism (mod-PD) and more than 4 years from diagnosis. The diagnosis of PD followed the UK Brain Bank Clinical Criteria. The Movement Disorders Society-Unified Parkinson's Disease Rating Scale (MDS-UPDRS) motor part (III) was obtained for all patients in the off-medication state. In mild-PD and mod-PD groups, evaluations were performed after a minimum 12-h withdrawal of anti-parkinsonian drugs. All participants provided written informed consent according to local regulations. Demographic features are described in Table 1.

MRI acquisition and processing
MRI acquisition was performed with a hybrid 3T mMR-Biograph system (Siemens Healthcare, Erlangen, Germany). The MRI protocol included: (a) A 3D T1-weighted (T1w) magnetization-prepared rapid acquisition gradient echo (MPRAGE) sequence (TR/TE: 2300/3.34 ms; flip angle: 12°; FoV: 256 mm; in-plane matrix: 256×256; in-plane resolution: 1×1 mm^2; slice thickness: 1 mm; 176 sagittal slices); (b) A 3D multi-echo gradient echo (multi-GRE) sequence (TR: 60 ms; TEs: [4.36:4.64:46.12] ms; flip angle: 20°; FoV: 230 mm; in-plane matrix: 256×256; in-plane resolution: 0.9×0.9 mm^2; slice thickness: 2 mm; 60 slices).

DICOM data were converted to NIFTI format using the dcm2niix package[92]. T1w acquisitions were corrected for intensity bias[93], skull stripped with BET-FSL (FMRIB Software Library) v6.0[94,95], and nonlinearly registered to the ICBM-152 2009c Nonlinear Symmetric template (ICBM-152) by affine transformation followed by diffeomorphic symmetric normalization[96]. R2* relaxometry maps were reconstructed from magnitude multi-GRE images and estimated by applying nonlinear fitting of the

Table 1 | Demographic data

	HC (*n* = 20)	dn-PD (*n* = 28)	mild-PD (*n* = 15)	mod-PD (*n* = 26)
Age[a]	50.35 ± 11.02	55.44 ± 9.46	56.95 ± 8.77	56.61 ± 10.67
Sex (men/women)	10/10	16/12	9/6	16/10
Hand Dominance (R/L)	18/2	24/4	14/1	26/0
Side of onset (R/L)	–	19/9	9/6	16/10
Time from diagnosis (months)[a]	–	6.28 ± 3.78[c,d]	30.37 ± 3.33[b,d]	93.68 ± 26.57[b,c]
LEDD (mg/day)[a]	–	107.26 ± 103.42[c,d]	268.00 ± 270.59[b,d]	771.86 ± 258.84[b,c]
Total MDS-UPDRS III[a]	–	18.25 ± 8.67[d]	23.67 ± 8.97[d]	37.29 ± 8.09[b,c]
MAS - MDS-UPDRS III[a]	–	11.14 ± 4.33[d]	13.67 ± 4.06[d]	19.21 ± 3.86[b,c]
LAS - MDS-UPDRS III[a]	–	2.11 ± 3.12[d]	3.33 ± 2.97[d]	7.70 ± 3.21[b,c]

MAS more affected side, *LAS* less affected side.
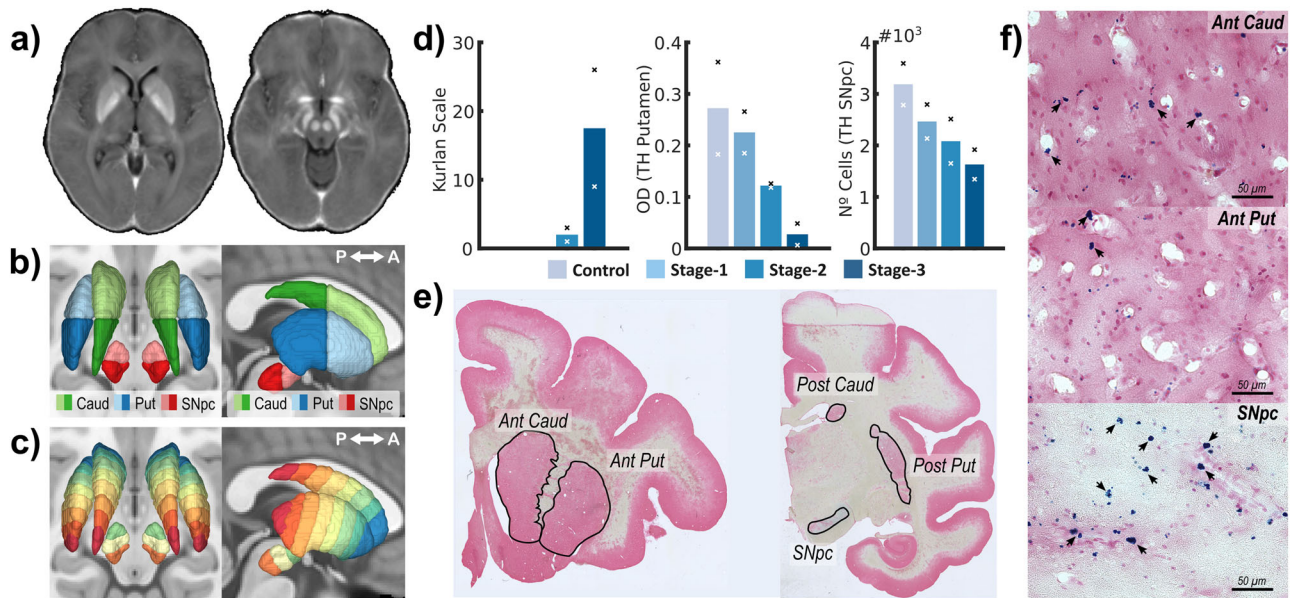[a]Mean value ± standard deviation.

Fig. 5 | Methodological figure. a Illustrative template built from the R2* MRI data of the HC group. Here, structures containing high iron concentrations, such as the substantia nigra, the striatum, the globus pallidus, or the red nucleus can clearly be seen. **b** Anterior and posterior ROIs in the caudate (green), putamen (blue), and SNpc (red). **c** PCA-ROI based divisions along the anteroposterior axis of the caudate, putamen, and SNpc. **d** Staging of the macaque groups according to their motor score (left), their dopaminergic decline in the putamen (center), the number of TH-positive neurons in the SNpc (right). Crosses denote the measurements obtained for each animal (**e**) Illustrative tissue slices in a control monkey showing the ROIs studied (**f**) Illustrative figures displaying iron cluster marked with Perls' Prussian blue staining.

complex monoexponential equation with an autoregressive algorithm[97] (Fig. 5a). Magnitude image from the first echo was used to rigidly register R2* maps to T1w space. Coregistration stages were conducted with ANTs (Advanced Registration Tools) v2.3.1[98].

Whole-caudate and whole-putamen segmentations were extracted from structural T1w images applying the FMRIB integrated registration and segmentation tool (FIRST)[99]. Both nuclei were partitioned into pre- and post-commissural divisions applying a vertical cutting plane that was set across the anterior commissure (Fig. 5b). A whole-SNpc mask was extracted from a reference atlas[100] (Prob. ≥ 0.001) and partitioned into anteromedial/posterolateral ROIs using the centroid of the red nucleus as reference (also extracted from the previous atlas). In order to enhance our characterization of the iron trends across these nuclei, a PCA was applied to determine the axis that better fits the morphology of each nucleus[30,31]. This axis, primarily aligned along the posteroanterior direction, was used to split these nuclei into multiple segments of equal thickness. The caudate and putamen were divided into 8 slices, whereas the SNpc was divided into 3 cuts (Fig. 5c). The first slice of the caudate (the posterior part of its tail) was excluded from the study, as it included very few voxels to perform reliable quantification. To keep symmetry between hemispheres in our atlas-based ROIs, SNpc segmentations were defined from left hemisphere mask and subsequently mirrored in ICBM-152 template space. All ROI masks were transformed to native R2* space applying a nearest-neighbor interpolation strategy and used to assess the mean signal within these ROIs.

PET imaging and processing
PET data were available only for dn-PD and mild-PD groups and were acquired simultaneously to the MRI acquisition. PET scans were carried out with subjects at rest and after a minimum of 6-hours of fasting. Patients receiving antiparkinsonian medication had their treatment suspended at least 48 h before PET acquisition. Scans were acquired for 90 min in list-mode immediately after an intravenous injection of ~5 mCi of FDOPA. PET images were reconstructed using an ordered subset-expectation max-imization algorithm, smoothed by applying a 3D isotropic Gaussian kernel with 4 mm full width at half maximum, and then corrected for attenuation with a 4-compartment MR-based map derived from a dual-echo Dixon-

based sequence (TR: 3.6 ms; TE: [1.23,2.46] ms), which incorporates bone information through a model-based segmentation algorithm[101]. A total of twenty-two activity timeframes were reconstructed (10 frames of 90 s, 9 frames of 300 s, and 3 frames of 600 s) with an effective resolution of $2.09 \times 2.09 \times 2.03$ mm^3. These activity frames were realigned within subjects computing rigid-body transformations with Mc-FLIRT-FSL[102]. Voxel-based FDOPA uptake rate maps (described as constant K_i [min^{-1}]) were estimated applying the Patlak graphical method[103]. An average time-activity curve from an occipital lobe mask was used as a reference in this approach. FDOPA K_i values were evaluated in the putamen and the SNpc in order to test the correlation between iron and dopaminergic alterations.

Non-human primate groups
Brain tissue from eight male macaca fascicularis (weight: 8–12 kg; age: 7–10 years) sourced from R.C. Hartelust BV (Tilburg, The Netherlands) were used for the histological study. Six monkeys received systemic administration (i.v.) of MPTP under light anesthetic conditions (ketamine 10 mg/kg; i.m.). Neurotoxic MPTP doses (0.5 mg/kg every 2 weeks) were administered to induce slow and progressive degeneration within the nigrostriatal dopaminergic system[104]. The number of injections varied depending on each animal's systemic response, up to a maximum of 3 MPTP doses. After the MPTP protocol, two monkeys exhibited evident parkinsonian signs, two animals only displayed mild signs, and the last two showed no apparent parkinsonism. The remaining two macaques were used as controls and only received saline. Thus, animals were grouped in cohorts of two monkeys (control and stages 1 to 3 of neurodegeneration) according to motor signs. This nomenclature was used to avoid confusion with human PD groups. The motor score was assessed with the Kurlan motor scale[105]. In order to verify the performance of the MPTP-model, nigrostriatal degeneration was quantified through the TH immunohistochemistry in both putamen (optical density) and SNpc (number of TH-positive neurons). Both metrics correlated with parkinsonian signs in agreement with previous literature[28,29] (Fig. 5d). All animals were housed and treated in accordance with the European and Spanish guidelines for animal care (86/609/EEC and 2003/65/EC European Council Directives and the Spanish Government). The experimental protocol was approved by the Ethical Committee for Research

of the Fundación de Investigación HM Hospitales and of Comunidad de Madrid (Spain).

Tissue processing, stereology, and iron load quantification

Macaques were sacrificed from 2 to 14 weeks after receiving the last MPTP dose. Prior to sacrifice, animals were deeply anesthetized with sodium pentobarbital (10 mg/kg/i.p.). Following anesthetic delivery, monkeys were perfused through the ascending aorta with saline, followed by 4% paraformaldehyde in phosphate buffer (PB) and a series of PB sucrose solutions (5–10–20%). Brains were sectioned in coronal slices on a freezing microtome at 40 μm to produce 10 matched series. The number of TH-positive neurons in the SNpc and striatal optical density of TH immunostaining were assessed as previously described[72].

The histological detection of ferric iron (Fe^{3+}) was performed with an iron stain kit (ab150674, Perls' Prussian blue stain; PPB) from Abcam following the manufacturer's specifications. Iron staining was performed on seven sections regularly spaced at intervals of 2400 μm, covering the entire anteroposterior axis of the striatum and five sections regularly spaced at intervals of 1200 μm, covering the entire anteroposterior axis of the SNpc. Briefly, sections were first mounted on gelatin-subbed glass slides and incubated for 5 min with equal parts of potassium ferrocyanide solution and hydrochloric acid solutions. They were then washed several times in distilled water and counterstained for 10 min with Nuclear Fast Red. Finally, brain sections were dehydrated and coverslipped.

Caudate and putamen structures were visually identified via Fast Red counterstain (see Fig. 5d). Analogous to the MRI study, both nuclei were partitioned into anterior and posterior ROIs using the anterior commissure as reference (Fig. 5e). The SNpc was also visually recognized using both PPB and Fast Red staining (see Fig. 5d). Since no red nucleus centroid could be identified, the whole-SNpc was studied as a single ROI (Fig. 5e). Multiple frames were acquired across each ROI, mapping the whole area with a 500 μm spacing grid. All frames were acquired using a bright field microscope (DM 2500; Leica, Wetzlar, Germany) at 40× magnification (Fig. 5f).

Each frame underwent preprocessing to aid in iron quantification (see Supplementary Fig. 3). First, images were divided into RGB components. An initial iron-negative mask was then generated by automated thresholding using the isolated red channel (Intermodes in ImageJ/Fiji)[106]. Subsequently, red and blue channels were inverted to bring intensities in iron clusters to maximum values. In order to approximate background pixels to zero intensities and remove the Fast Red counterstaining contribution to those pixels stained with PPB, each channel was truncated after subtracting the mean value within the negative-iron mask. Following this, a positive-iron mask was defined by automated thresholding[106] using the preprocessed red channel. This mask was employed to quantify iron in the preprocessed blue channel. Optical density (OD) and area percent covered by blue staining (AP) were extracted from each frame, reflecting the density within the iron clusters and the extension of these clusters respectively (Analyze particles in ImageJ/Fiji). Both metrics were averaged across frames within region boundaries and across section slices to obtain a single value per animal and ROI. For simplicity, we developed a third metric named relative integrated density (RID), by combining both OD and AP, and reflecting the rate of change normalized to control animals. This was calculated by first normalizing both metrics to the mean value within the ROI of interest of the control group, and then averaging both normalized metrics:

$$RID_f = \frac{1}{2}\left(\frac{OD_f}{OD_{Cont}} + \frac{AP_f}{AP_{Cont}}\right) \tag{1}$$

where RID_f, OD_f and AP_f are, respectively the RID, the OD, and the AP within the ROI for the frame being studied, and OD_{Cont} and AP_{Cont} are the mean OD and the mean AP of the control group within the ROI. Accordingly, a value of RID < 1 would reflect a reduction of iron levels compared to control animals and vice versa. Image pre-processing and quantification steps were performed with ImageJ/Fiji v.1.53[107].

Statistical analyses

For the neuroimaging study, mean ROI values were arranged by side according to the predominance of motor signs (PD) or hand dominance (HC), i.e., more and less affected sides (MAS and LAS respectively) or dominant and non-dominant sides (DS and nDS). Mann–Whitney U tests were conducted for MAS (DS in HC) and LAS (nDS in HC) separately in order to identify differences between groups. Since dn-PD and mild-PD cohorts partially involve the same subjects, group comparisons were restricted to those subjects included in both groups, and differences were assessed with paired Mann–Whitney U tests. Complementary to *P*-values, Cohen *d* was used to evaluate the effect size and Bayes factors (BF) were computed to quantify the strength of evidence against the null hypothesis (no differences). These BF were described on a logarithmic scale ($K = log_{10}(BF)$)[108]. Combining both Classical and Bayesian Statistics frameworks, the following categorization was adopted to describe significances: $P < 0.05$ and $K \geq 0$ (weak significance), $P < 0.05$ and $0.5 < K \leq 1$ (moderate significance); $P \leq 0.01$ and $K > 1$ (strong significance). Relations between iron and dopamine alterations were studied with non-parametric Spearman correlation analyses between R2* and FDOPA K_i values in SNpc and putamen.

In the animal cohorts, and due to the small size of the sample, only Descriptive Statistics (mean) were used to analyze the data in the histological study. In addition, to assess the relationship between iron and dopaminergic alterations, non-parametric Spearman correlation analyses were performed between the histologic metrics assessed on each ROI and the TH quantification in the whole putamen and the SNpc. All statistics were computed with MATLAB (The MathWorks Inc., United States).

Data availability

The data supporting these study findings are available from the corresponding author upon request by any qualified investigator.

Code availability

Image processing packages are freely available in their respective websites: dcm2niix: https://github.com/rordenlab/dcm2niix; FSL v6.0: https://fsl.fmrib.ox.ac.uk/fsl/fslwiki/FSL; ANTs: http://stnava.github.io/ANTs/; ImageJ/Fiji v1.53: https://imagej.net/software/fiji/; MEDI Toolbox: https://pre.weill.cornell.edu/mri/pages/qsm.html; In-house MATLAB and ImageJ codes developed for the statistical analyses are available to any qualified researcher from the corresponding author.

References

1. Bernheimer, H., Birkmayer, W., Hornykiewicz, O., Jellinger, K. & Seitelberger, F. Brain dopamine and the syndromes of Parkinson and Huntington Clinical, morphological and neurochemical correlations. *J. Neurological Sci.* **20**, 415–455 (1973).
2. Kish, S. J., Shannak, K. & Hornykiewicz, O. Uneven Pattern of Dopamine Loss in the Striatum of Patients with Idiopathic Parkinson's Disease. *N. Engl. J. Med.* **318**, 876–880 (1988).
3. Fearnley, J. M. & Lees, A. J. Ageing and Parkinson's disease: substantia nigra regional selectivity. *Brain* **114**, 2283–2301 (1991).
4. Damier, P., Hirsch, E. C., Agid, Y. & Graybiel, A. M. The substantia nigra of the human brain. *Brain* **122**, 1437–1448 (1999).
5. Zecca, L. et al. The role of iron and copper molecules in the neuronal vulnerability of locus coeruleus and substantia nigra during aging. *Proc. Natl Acad. Sci. USA* **101**, 9843–9848 (2004).
6. Zucca, F. A. et al. Interactions of iron, dopamine and neuromelanin pathways in brain aging and Parkinson's disease. *Prog. Neurobiol.* **155**, 96–119 (2017).
7. Gaasch, J. A., Lockman, P. R., Geldenhuys, W. J., Allen, D. D. & Van Der Schyf, C. J. Brain Iron Toxicity: Differential Responses of

Astrocytes, Neurons, and Endothelial Cells. *Neurochem. Res.* **32**, 1196–1208 (2007).

8. Dixon, S. J. et al. Ferroptosis: An Iron-Dependent Form of Nonapoptotic Cell Death. *Cell* **149**, 1060–1072 (2012).

9. Blesa, J., Trigo-Damas, I., Quiroga-Varela, A. & Jackson-Lewis, V. R. Oxidative stress and Parkinson's disease. *Front. Neuroanat* **9**, 91 (2015).

10. Morris, C. M. & Edwardson, J. A. Iron histochemistry of the substantia nigra in Parkinson's disease. *Neurodegeneration* **3**, 277–282 (1994).

11. Zecca, L. et al. In vivo detection of iron and neuromelanin by transcranial sonography: A new approach for early detection of substantia nigra damage. *Mov. Disord.* **20**, 1278–1285 (2005).

12. Ulla, M. et al. Is R2* a New MRI Biomarker for the Progression of Parkinson's Disease? A Longitudinal Follow-Up. *PLoS ONE* **8**, e57904 (2013).

13. Langkammer, C. et al. Quantitative Susceptibility Mapping in Parkinson's Disease. *PLoS ONE* **11**, e0162460 (2016).

14. Bergsland, N. et al. Ventral posterior substantia nigra iron increases over 3 years in Parkinson's disease. *Mov. Disord.* **34**, 1006–1013 (2019).

15. Murakami, Y. et al. Usefulness of Quantitative Susceptibility Mapping for the Diagnosis of Parkinson Disease. *AJNR Am. J. Neuroradiol.* **36**, 1102–1108 (2015).

16. Du, G. et al. Dynamics of Nigral Iron Accumulation in Parkinson's Disease: From Diagnosis to Late Stage. *Mov. Disord.* **37**, 1654–1662 (2022).

17. Gille, G. & Reichmann, H. Iron-dependent functions of mitochondria—relation to neurodegeneration. *J. Neural Transm.* **118**, 349–359 (2011).

18. Ndayisaba, A., Kaindlstorfer, C. & Wenning, G. K. Iron in Neurodegeneration – Cause or Consequence? *Front. Neurosci.* **13**, 180 (2019).

19. Hopes, L. et al. Magnetic Resonance Imaging Features of the Nigrostriatal System: Biomarkers of Parkinson's Disease Stages? *PLoS ONE* **11**, e0147947 (2016).

20. Ravanfar, P. et al. Systematic Review: Quantitative Susceptibility Mapping (QSM) of Brain Iron Profile in Neurodegenerative Diseases. *Front. Neurosci.* **15**, 618435 (2021).

21. Erikson, K. M., Jones, B. C. & Beard, J. L. Iron Deficiency Alters Dopamine Transporter Functioning in Rat Striatum. *J. Nutr.* **130**, 2831–2837 (2000).

22. Erikson, K. M., Jones, B. C., Hess, E. J., Zhang, Q. & Beard, J. L. Iron deficiency decreases dopamine D1 and D2 receptors in rat brain. *Pharmacol. Biochem. Behav.* **69**, 409–418 (2001).

23. Bianco, L. E., Wiesinger, J., Earley, C. J., Jones, B. C. & Beard, J. L. Iron deficiency alters dopamine uptake and response to L-DOPA injection in Sprague–Dawley rats. *J. Neurochem.* **106**, 205–215 (2008).

24. Matak, P. et al. Disrupted iron homeostasis causes dopaminergic neurodegeneration in mice. *Proc. Natl Acad. Sci. USA* **113**, 3428–3435 (2016).

25. Cheng, Q. et al. Evaluation of abnormal iron distribution in specific regions in the brains of patients with Parkinsonas disease using quantitative susceptibility mapping and R2* mapping. *Exp. Ther. Med* **19**, 3778–3786 (2020).

26. Langley, J., Huddleston, D. E. & Hu, X. Nigral diffusivity, but not free water, correlates with iron content in Parkinson's disease. *Brain Commun.* **3**, fcab251 (2021).

27. Langkammer, C. et al. Quantitative MR Imaging of Brain Iron: A Postmortem Validation Study. *Radiology* **257**, 455–462 (2010).

28. Blesa, J. et al. Progression of dopaminergic depletion in a model of MPTP-induced Parkinsonism in non-human primates. An 18F-DOPA and 11C-DTBZ PET study. *Neurobiol. Dis.* **38**, 456–463 (2010).

29. Porras, G., Li, Q. & Bezard, E. Modeling Parkinson's Disease in Primates: The MPTP Model. *Cold Spring Harb. Perspect. Med.* **2**, a009308–a009308 (2012).

30. Drori, E., Berman, S. & Mezer, A. A. Mapping microstructural gradients of the human striatum in normal aging and Parkinson's disease. *Sci. Adv.* **8**, eabm1971 (2022).

31. Berman, S., Drori, E. & Mezer, A. A. Spatial profiles provide sensitive MRI measures of the midbrain micro- and macrostructure. *NeuroImage* **264**, 119660 (2022).

32. Pyatigorskaya, N. et al. Iron Imaging as a Diagnostic Tool for Parkinson's Disease: A Systematic Review and Meta-Analysis. *Front. Neurol.* **11**, 366 (2020).

33. Du, G. et al. Combined R2* and Diffusion Tensor Imaging Changes in the Substantia Nigra in Parkinson's Disease: Iron AND FA Changes IN SN OF PD Patients. *Mov. Disord.* **26**, 1627–1632 (2011).

34. Guan, X. et al. Regionally progressive accumulation of iron in Parkinson's disease as measured by quantitative susceptibility mapping: Regionally progressive accumulation of iron in Parkinson's disease. *NMR Biomed.* **30**, e3489 (2017).

35. Depierreux, F. et al. Parkinson's disease multimodal imaging: F-DOPA PET, neuromelanin-sensitive and quantitative iron-sensitive MRI. *npj Parkinsons Dis.* **7**, 57 (2021).

36. Sofic, E. et al. Increased iron (III) and total iron content in post mortem substantia nigra of parkinsonian brain. *J. Neural Transm.* **74**, 199–205 (1988).

37. Dexter, D. T. et al. Increased Nigral Iron Content and Alterations in Other Metal Ions Occurring in Brain in Parkinson's Disease. *J. Neurochem* **52**, 1830–1836 (1989).

38. Riederer, P. et al. Transition Metals, Ferritin, Glutathione, and Ascorbic Acid in Parkinsonian Brains. *J. Neurochem* **52**, 515–520 (1989).

39. Griffiths, P. D. & Crossman, A. R. Distribution of Iron in the Basal Ganglia and Neocortex in Postmortem Tissue in Parkinson's Disease and Alzheimer's Disease. *Dement Geriatr. Cogn. Disord.* **4**, 61–65 (1993).

40. Dexter, D. T. et al. Alterations in the levels of iron, ferritin and other trace metals in Parkinson's disease and other neurodegenerative diseases affecting the basal ganglia. *Brain* **114**, 1953–1975 (1991).

41. He, Y. et al. Dopaminergic cell death precedes iron elevation in MPTP-injected monkeys. *Free Radic. Biol. Med.* **35**, 540–547 (2003).

42. Salazar, J. et al. Divalent metal transporter 1 (DMT1) contributes to neurodegeneration in animal models of Parkinson's disease. *Proc. Natl Acad. Sci. USA* **105**, 18578–18583 (2008).

43. Dexter, D. T. et al. Decreased Ferritin Levels in Brain in Parkinson's Disease. *J. Neurochem.* **55**, 16–20 (1990).

44. Faucheux, B. A., Hauw, J.-J., Agid, Y. & Hirsch, E. C. The density of [125I]-transferrin binding sites on perikarya of melanized neurons of the substantia nigra is decreased in Parkinson's disease. *Brain Res.* **749**, 170–174 (1997).

45. Zhang, N., Yu, X., Xie, J. & Xu, H. New Insights into the Role of Ferritin in Iron Homeostasis and Neurodegenerative Diseases. *Mol. Neurobiol.* **58**, 2812–2823 (2021).

46. Wang, J., Jiang, H. & Xie, J. Ferroportin1 and hephaestin are involved in the nigral iron accumulation of 6-OHDA-lesioned rats. *Eur. J. Neurosci.* **25**, 2766–2772 (2007).

47. Song, N., Wang, J., Jiang, H. & Xie, J. Ferroportin 1 but not hephaestin contributes to iron accumulation in a cell model of Parkinson's disease. *Free Radic. Biol. Med.* **48**, 332–341 (2010).

48. Shi, L. et al. The Association of Iron and the Pathologies of Parkinson's Diseases in MPTP/MPP+-Induced Neuronal Degeneration in Non-human Primates and in Cell Culture. *Front. Aging Neurosci.* **11**, 215 (2019).

49. Li, K. R. et al. Quantitative evaluation of brain iron accumulation in different stages of Parkinson's disease. *J. Neuroimaging* **32**, 363–371 (2022).

50. Péran, P. et al. Magnetic resonance imaging markers of Parkinson's disease nigrostriatal signature. *Brain* **133**, 3423–3433 (2010).

51. Barbosa, J. H. O. et al. Quantifying brain iron deposition in patients with Parkinson's disease using quantitative susceptibility mapping, R2 and R2*. *Magn. Reson. Imaging* **33**, 559–565 (2015).

52. Acosta-Cabronero, J. et al. The whole-brain pattern of magnetic susceptibility perturbations in Parkinson's disease. *Brain* **140**, 118–131 (2017).

53. Martin-Bastida, A. et al. Motor associations of iron accumulation in deep grey matter nuclei in Parkinson's disease: a cross-sectional study of iron-related magnetic resonance imaging susceptibility. *Eur. J. Neurol.* **24**, 357–365 (2017).

54. Fu, X. et al. Time-Specific Pattern of Iron Deposition in Different Regions in Parkinson's Disease Measured by Quantitative Susceptibility Mapping. *Front. Neurol.* **12**, 631210 (2021).

55. Xuan, M. et al. Different iron deposition patterns in early- and middle-late-onset Parkinson's disease. *Parkinsonism Relat. Disord.* **44**, 23–27 (2017).

56. Graham, J. M. Brain iron deposition in Parkinson's disease imaged using the PRIME magnetic resonance sequence. *Brain* **123**, 2423–2431 (2000).

57. Esterhammer, R. et al. Potential of Diffusion Tensor Imaging and Relaxometry for the Detection of Specific Pathological Alterations in Parkinson's Disease (PD). *PLoS ONE* **10**, e0145493 (2015).

58. Chen, Q. et al. Iron deposition in Parkinson's disease by quantitative susceptibility mapping. *BMC Neurosci.* **20**, 23 (2019).

59. Pichler, I. et al. Serum Iron Levels and the Risk of Parkinson Disease: A Mendelian Randomization Study. *PLoS Med.* **10**, e1001462 (2013).

60. Genoud, S., Senior, A. M., Hare, D. J. & Double, K. L. Meta-Analysis of Copper and Iron in Parkinson's Disease Brain and Biofluids. *Mov. Disord.* **35**, 662–671 (2020).

61. Shen, X., Yang, H., Zhang, D. & Jiang, H. Iron Concentration Does Not Differ in Blood but Tends to Decrease in Cerebrospinal Fluid in Parkinson's Disease. *Front. Neurosci.* **13**, 939 (2019).

62. Logroscino, G., Chen, H., Wing, A. & Ascherio, A. Blood donations, iron stores, and risk of Parkinson's disease. *Mov. Disord.* **21**, 835–838 (2006).

63. Hong, C. T. et al. Newly Diagnosed Anemia Increases Risk of Parkinson's disease: A Population-Based Cohort Study. *Sci. Rep.* **6**, 29651 (2016).

64. Wang, Y.-C. et al. Association between Anemia and Risk of Parkinson Disease. *Behav. Neurol.* **1**, 8 (2021).

65. Beard, J. L., Chen, Q., Connor, J. & Jones, B. C. Altered monamine metabolism in caudate-putamen of iron-deficient rats. *Pharmacol. Biochem. Behav.* **48**, 621–624 (1994).

66. Brück, A. et al. A follow-up study on 6-[^{18}F]fluoro-L-dopa uptake in early Parkinson's disease shows nonlinear progression in the putamen: Striatal Fdopa Uptake in Parkinson's Disease. *Mov. Disord.* **24**, 1009–1015 (2009).

67. Oh, M. et al. Subregional Patterns of Preferential Striatal Dopamine Transporter Loss Differ in Parkinson Disease, Progressive Supranuclear Palsy, and Multiple-System Atrophy. *J. Nucl. Med.* **53**, 399–406 (2012).

68. Pineda-Pardo, J. A., Sánchez-Ferro, Á., Monje, M. H. G., Pavese, N. & Obeso, J. A. Onset pattern of nigrostriatal denervation in early Parkinson's disease. *Brain* **145**, 1018–1028 (2022).

69. López-Aguirre, M. et al. Dopaminergic denervation and associated MRI microstructural changes in the nigrostriatal projection in early Parkinson's disease patients. *npj Parkinsons Dis.* **9**, 144 (2023).

70. Devos, D. et al. Trial of Deferiprone in Parkinson's Disease. *N. Engl. J. Med.* **387**, 2045–2055 (2022).

71. Nandhagopal, R. et al. Longitudinal evolution of compensatory changes in striatal dopamine processing in Parkinson's disease. *Brain* **134**, 3290–3298 (2011).

72. Blesa, J. et al. The nigrostriatal system in the presymptomatic and symptomatic stages in the MPTP monkey model: A PET, histological and biochemical study. *Neurobiol. Dis.* **48**, 79–91 (2012).

73. Kaasinen, V. & Vahlberg, T. Striatal dopamine in Parkinson disease: A meta-analysis of imaging studies. *Ann. Neurol.* **82**, 873–882 (2017).

74. Hauser, R. A. Levodopa: Past, Present, and Future. *Eur. Neurol.* **62**, 1–8 (2009).

75. Xu, H. et al. New Progress on the Role of Glia in Iron Metabolism and Iron-Induced Degeneration of Dopamine Neurons in Parkinson's Disease. *Front. Mol. Neurosci.* **10**, 455 (2018).

76. Reinert, A., Morawski, M., Seeger, J., Arendt, T. & Reinert, T. Iron concentrations in neurons and glial cells with estimates on ferritin concentrations. *BMC Neurosci.* **20**, 25 (2019).

77. Cheli, V. T., Correale, J., Paez, P. M. & Pasquini, J. M. Iron Metabolism in Oligodendrocytes and Astrocytes, Implications for Myelination and Remyelination. *ASN Neuro* **12**, 175909142096268 (2020).

78. Basurco, L. et al. Microglia and astrocyte activation is region-dependent in the α-synuclein mouse model of Parkinson's disease. *Glia* **71**, 571–587 (2023).

79. Weiss, F., Labrador-Garrido, A., Dzamko, N. & Halliday, G. Immune responses in the Parkinson's disease brain. *Neurobiol. Dis.* **168**, 105700 (2022).

80. Ramos, P. et al. Iron levels in the human brain: A post-mortem study of anatomical region differences and age-related changes. *J. Trace Elem. Med. Biol.* **28**, 13–17 (2014).

81. Acosta-Cabronero, J., Betts, M. J., Cardenas-Blanco, A., Yang, S. & Nestor, P. J. In Vivo MRI Mapping of Brain Iron Deposition across the Adult Lifespan. *J. Neurosci.* **36**, 364–374 (2016).

82. Li, G. et al. Age-dependent changes in brain iron deposition and volume in deep gray matter nuclei using quantitative susceptibility mapping. *NeuroImage* **269**, 119923 (2023).

83. Haacke, E. M. et al. Imaging iron stores in the brain using magnetic resonance imaging. *Magn. Reson. Imaging* **23**, 1–25 (2005).

84. Punwani, S. et al. Correlation between Absolute Deoxyhaemoglobin [dHb] Measured by Near Infrared Spectroscopy (NIRS) and Absolute R2′ as Determined by Magnetic Resonance Imaging (MRI). In: *Optical Imaging of Brain Function and Metabolism 2* (eds. Villringer, A. & Dirnagl, U.) 413, 129–137 (Springer, 1997).

85. Mitsumori, F., Watanabe, H. & Takaya, N. Estimation of brain iron concentration in vivo using a linear relationship between regional iron and apparent transverse relaxation rate of the tissue water at 4.7T: In Vivo Iron Meter for Human Brain. *Magn. Reson. Med.* **62**, 1326–1330 (2009).

86. Fukunaga, M. et al. Layer-specific variation of iron content in cerebral cortex as a source of MRI contrast. *Proc. Natl Acad. Sci. USA* **107**, 3834–3839 (2010).

87. Du, G. et al. Quantitative susceptibility mapping of the midbrain in Parkinson's disease: Nigral Iron in PD. *Mov. Disord.* **31**, 317–324 (2016).

88. Rua, C. et al. Multi-centre, multi-vendor reproducibility of 7T QSM and R2* in the human brain: Results from the UK7T study. *NeuroImage* **223**, 117358 (2020).

89. Thomas, G. E. C. et al. Brain iron deposition is linked with cognitive severity in Parkinson's disease. *J. Neurol. Neurosurg. Psychiatry* **91**, 418–425 (2020).

90. Martínez-Fernández, R. et al. Randomized Trial of Focused Ultrasound Subthalamotomy for Parkinson's Disease. *N. Engl. J. Med* **383**, 2501–2513 (2020).

91. Monje, M. H. G. et al. Motor Onset Topography and Progression in Parkinson's Disease: the Upper Limb Is First. *Mov. Disord.* **36**, 905–915 (2021).

92. Li, X., Morgan, P. S., Ashburner, J., Smith, J. & Rorden, C. The first step for neuroimaging data analysis: DICOM to NIfTI conversion. *J. Neurosci. Methods* **264**, 47–56 (2016).

93. Tustison, N. J. et al. N4ITK: Improved N3 Bias Correction. *IEEE Trans. Med. Imaging* **29**, 1310–1320 (2010).

94. Smith, S. M. Fast robust automated brain extraction. *Hum. Brain Mapp.* **17**, 143–155 (2002).

95. Jenkinson, M., Beckmann, C. F., Behrens, T. E. J., Woolrich, M. W. & Smith, S. M. FSL. *NeuroImage* **62**, 782–790 (2012).

96. Avants, B., Epstein, C., Grossman, M. & Gee, J. Symmetric diffeomorphic image registration with cross-correlation: Evaluating automated labeling of elderly and neurodegenerative brain. *Med. Image Anal.* **12**, 26–41 (2008).

97. Pei, M. et al. Algorithm for fast monoexponential fitting based on Auto-Regression on Linear Operations (ARLO) of data: T2* Mapping Using ARLO. *Magn. Reson. Med.* **73**, 843–850 (2015).

98. Avants, B. B. et al. A reproducible evaluation of ANTs similarity metric performance in brain image registration. *NeuroImage* **54**, 2033–2044 (2011).

99. Patenaude, B., Smith, S. M., Kennedy, D. N. & Jenkinson, M. A Bayesian model of shape and appearance for subcortical brain segmentation. *NeuroImage* **56**, 907–922 (2011).

100. Pauli, W. M., Nili, A. N. & Tyszka, J. M. A high-resolution probabilistic in vivo atlas of human subcortical brain nuclei. *Sci. Data* **5**, 180063 (2018).

101. Paulus, D. H. et al. Whole-Body PET/MR Imaging: Quantitative Evaluation of a Novel Model-Based MR Attenuation Correction Method Including Bone. *J. Nucl. Med.* **56**, 1061–1066 (2015).

102. Jenkinson, M., Bannister, P., Brady, M. & Smith, S. Improved Optimization for the Robust and Accurate Linear Registration and Motion Correction of Brain Images. *NeuroImage* **17**, 825–841 (2002).

103. Patlak, C. S., Blasberg, R. G. & Fenstermacher, J. D. Graphical Evaluation of Blood-to-Brain Transfer Constants from Multiple-Time Uptake Data. *J. Cereb. Blood Flow. Metab.* **3**, 1–7 (1983).

104. Del Rey, N. L.-G. et al. Calbindin and Girk2/Aldh1a1 define resilient vs vulnerable dopaminergic neurons in a primate Parkinson's disease model. *npj Parkinsons Dis.* **10**, 165 (2024).

105. Kurlan, R., Kim, M. H. & Gash, D. M. Oral levodopa dose-response study in MPTP-induced hemiparkinsonian monkeys: Assessment with a new rating scale for monkey parkinsonism. *Mov. Disord.* **6**, 111–118 (1991).

106. Prewitt, J. M. S. & Mendelsohn, M. L. The analysis of cell images. *Ann. N. Y. Acad. Sci.* **128**, 1035–1053 (1966).

107. Schindelin, J. et al. Fiji: an open-source platform for biological-image analysis. *Nat. Methods* **9**, 676–682 (2012).

108. Kass, R. E. & Raftery, A. E. Bayes Factors. *J. Am. Stat. Assoc.* **90**, 773–795 (1995).

Acknowledgements

Author contributions

M.L.A.: Conceptualization of the study, methodological design, histologic quantification, software development, formal analysis, manuscript writing, and figure editing; T.B.: Methodological design, histologic quantification, and manuscript consulting/advice; M.H.G.M.: Neurological examinations, PD patient recruitment, and manuscript consulting/advice; N.E.G.: Methodological design and manuscript consulting/advice; R.M.F.: Neurological examinations, PD patient recruitment, and manuscript consulting/advice; N.L.G.D.R.: Tissue processing and histologic quantification; M.C.: Tissue processing; A.S.F.: Neurological examinations, PD patient recruitment, and manuscript consulting/advice; I.T.: Primate manipulation and manuscript consulting/advice; J.B.: Conceptualization of the study, methodological design, primate manipulation, and manuscript consulting/advisory; J.A.O.: Conceptualization of the study, methodological design, and manuscript writing; J.A.P.P.: Conceptualization of the study, methodological design, MRI data collection, and manuscript writing. All authors read and approved the final manuscript.

Competing interests

The authors declare no competing interests.

Additional information

Supplementary information The online version contains supplementary material available at https://doi.org/10.1038/s41531-025-00911-6.

Correspondence and requests for materials should be addressed to J. A. Pineda-Pardo.

Reprints and permissions information is available at http://www.nature.com/reprints

Publisher's note Springer Nature remains neutral with regard to jurisdictional claims in published maps and institutional affiliations.